# Phase Change Materials for on-chip signal modulation

*A THESIS*

*submitted by*

**VICTORIA VOINKOVA**

*for the award of the degree of*

**MASTER OF SCIENCE IN OPTICS AND PHOTONICS**

at Karlsruhe Institute of Technology, Germany

*Performed at* **Kirchhoff Institute of Physics**

*Supervised by* **Prof. Dr. Wolfram Pernice, KIP**

*Supervised by* **Dr. Prof. Uli Lemmer, KIT**

*Submitted on* **29th of October, 2024**

Karlsruher Institut für Technologie

KIRCHHOFF-INSTITUT FÜR PHYSIK

# ABSTRACT

KEYWORDS: Phase Changing Materials, Silicon on insulator device, Mach-Zender Interferometer, Interferometry, Optical memory

On-chip nonvolatile photonic memory would be a revolution in optoelectronic computing, reducing power consumption and accessing the multi-channel operations. The promising candidate for this role are Phase Changing Materials (PCM), which expose different optical properties depending on their phase, which can be manipulated. The well-studied PCM alloy $Ge_2Sb_2Te_5$ (GST) show the significant change in complex refractive index in visible and near-infrared wavelength region. The state discrimination down to nanoscale cell size is a key factor for miniaturisation of the devices and incorporating GST into the complex photonic computing architectures. Encoding of photonic memory is done via local phase switching of GST, which results in propagating signal modulation. In the scope of this work, the switching of PCM and effective signal modulation was evaluated. The new interferometric measurement method was introduced and implemented, its result made good comparison with previously used one.

# TABLE OF CONTENTS

# LIST OF FIGURES

# ABBREVIATIONS

| | |
|---|---|
| **CNN** | Convolutional Neural Network |
| **SOI** | Silicon on insulator |
| **PCM** | Phase Changing Materials |
| **GST** | $Ge_2Sb_3Te_5$ |
| **MZI** | Mach-Zender Interferometer |
| **DUT** | Device under test |
| **FSR** | Free Spectral Range |
| **ER** | Extinction ratio |
| **TF** | Transfer Function |
| **OSA** | Optical Spectrum Analyser |

# Declaration of Originality

I herewith declare that the present thesis is original work written by me alone, that I have indicated completely and precisely all aids used as well as all citations, whether changed or unchanged, of other theses and publications, and that I have observed the KIT Statutes for Upholding Good Scientific Practice, as amended.

# CHAPTER 1

# Introduction

The rapid evolution of computational technology has been driven by the increasing demand for processing large volumes of data, executing complex algorithms, and supporting real-time applications in various domains such as artificial intelligence (AI), scientific simulations, and high-performance computing (HPC) (Ben-Nun and Hoefler (2019)). However, as computational demands continue to grow, traditional hardware architectures face significant challenges in scaling to meet these requirements. The limitations of current processing units, memory architectures, and interconnect systems are becoming more apparent, hindering their ability to support the exponential growth in computational workloads (Feng and Xiao (2010), Kim and Jeong (2023)).

In recent years, the field of physical computing has made significant strides in addressing some of these challenges, particularly through the development of heterogeneous computing architectures and specialized processors (de Lima *et al.* (2017)). With those structures we can utilise diverse physical phenomena while facing specific challenges, making a direct connection between natural processes and the way of solving modern world problems. This parallel promises to be fruitful and has a big space for development, as, getting bigger computational power, we expand the understanding of natural phenomena themselves and can apply these knowledge for further enhancement. Nevertheless, creating physical hardware requires many stages of meticulous work and is being an emerging science field recently.

This work is devoted to the methods of evaluation of the structures, used in photonic hardware, – the building blocks of complex architectures. Through this exploration potential benefits and drawbacks of methods are highlighted,

providing insights into optimisation of such an essential step of creating physical computing hardware.

The thesis paper is organised as following: The Chapter 1 is giving a comprehensive overview of the scope of the problem and advocate for the main aim of this work. Chapter 2 describes the technical and theoretical perquisites, which were considered during the work. Chapter 3 presents step-by-step experimental process, giving complete information on all the operation parameters and intermediate working solutions. The work-flow of the experiment data analysis is also described in this chapter. Finally Chapter 4 concludes the acquired measurement information and presents the resulting overview of the evaluation methods of photonic structure of choice.

## 1.1 Challenges of modern computing

Conventional computing, with its reliance on general-purpose processors like Central Processing Units (CPUs), faces several significant challenges when dealing with the increasing demands of modern applications. Here is a brief observation of main of them.

One of the primary challenges is the **parallelism and scalability** of computing systems (Feldmann *et al.* (2021), Kim and Jeong (2023)). Modern hardware architectures widely rely on heterogeneous computing, which involves using different types of processors within the same system. Multi-core CPUs and GPUs have embraced parallelism, though efficiently utilizing these architectures for diverse computational tasks remains a challenge (Feng and Xiao (2010)). Many applications encounter issues related to synchronisation, memory contention, and communication bottlenecks. Robust and scalable parallelisation remains an aim to be achieved by more advanced mediators.

Additionally, **energy efficiency** of hardware systems present substantial hur-

dles. High-demanding computations, such as those in machine learning or large-scale simulations, require massive computational power, leading to increased energy consumption (Miller (2017)). As processors become more powerful, the energy required for both computation and data movement scales dramatically, posing a critical barrier to achieving sustainable computing at scale. Conventional processors are not designed with energy efficiency as a priority, which leads to higher operational costs, excessive heat generation, and the need for large-scale cooling solutions in data centers. To address energy inefficiency, Application-Specific Integrated Circuits (ASICs) and Field-Programmable Gate Arrays (FPGAs) are being employed (Jouppi (2017), Zhang *et al.* (2015)). Since they are optimized for a narrow range of functions, they use less power than general-purpose processors. Embedding these architectural solutions on physically energy efficient platform would contriibute to the mitigation of the energy crisis.

Moreover, **memory bandwidth and latency** are becoming bottlenecks in high-performance systems, putting the gap between fast processors and slower memory systems. Advanced applications, like large-scale simulations, scientific computing, and AI, require fast access to large datasets, yet traditional memory architectures struggle to keep up with the growing demand for low-latency, high-throughput data access. The performance gap between processing units and memory subsystems has led to inefficiencies, particularly in data-intensive applications. To address this, physical computing techniques leverage high-bandwidth memory and non-volatile memory technologies.

## 1.2 Photonic hardware

Physical computing has emerged as a response to the modern challenges, which are hardly maintained on electronic platform. Among other physical computing platforms, which have gained rapid development within last years, pho-

tonic computing stands out due to the several reasons. The primary advantage is a critical foundation of photonic devices investigation, provided by the development of optocommunication technology (Winzer *et al.* (2018)). Optocommunication, which involves the use of optical signals for data transmission in fiber-optic networks, has already demonstrated the capacity of light to transmit vast amounts of information over long distances with minimal latency. This technology, widely adopted in modern telecommunications, served as a key access point for integrating photonics into computing, showcasing the scalability, speed, and energy efficiency that light-based systems can offer. Building on these advancements, research in photonic computing aims to leverage similar principles at the processor level, enabling data to be processed and transmitted using optical circuits, which promise to revolutionize high-performance computing by eliminating many of the inefficiencies inherent in electronic systems (Miller (2017)). The feature of photonic platform is that all the benefits mentioned are tailored to the fundamental properties of light. Naturally addressing all the challenges simultaneously, light manipulation is highly profitable in long run. Unlike electrons, photons can travel at the speed of light and do not experience resistance in transmission, allowing for faster data processing and lower power consumption (de Lima *et al.* (2017)) For example, optical wire bonding has already proved beneficial, being deeply integrated in the most of the server systems (Optical Fiber and Data Centers: Powering the Digital Infrastructure). The heat losses attributed with the transmission in the optical fibers are significantly lower than those in analogous copper wires. Even combined with extra charges for electro-optical coding and decoding, it results in significant mitigation of heating effects. The long-haul high speed communication would not be possible without the light pulse propagation speed. The limiting factor here is the rate of electro-optical signal coding and decoding, which is tackled by introducing new ultra-fast photodiodes, developing new light modulation techniques and discovering new material platforms. The key factor contributing to the high performance of photonic devices is the inherent **parallelism** (Feldmann

*et al.* (2021)). Wide spectrum of light signals and advanced methods of spectral component separation and combining pave the way for the multi-channel operation. Dense Wavelength Division Multiplexing present the capacity of up to 160 channels on a single fiber, reaching Pbit/s **data transmission rates** (ECOC). For computing, more sparse frequency grid is needed to reduce parasitic effects, nevertheless operating in 192 channels have been reported (Di Pasquale *et al.* (2003)) for specific application, and this number is being constantly improved.

The peculiarity, worth mentioning from the beginning, is the high specialisation of the alternative hardware, which plays an ambiguous role. Designed for a specific task, this hardware is highly optimised and efficient (Miller (2017)), but introduce challenges in terms of programmability, flexibility, and integration with general-purpose hardware. These accelerators often require custom software stacks and tools, making it difficult for developers to harness their full potential across a wide range of applications. Due to this fact, the more reconfigurabile Field-Programmable Gate Arrays (FPGAs) has been widely investigated within the last years (Zhang *et al.* (2015)). Nonetheless, some computing application requires a very specific operation to be performed in the most efficient way.

### 1.2.1 Neuromorphic computing

Neural Networks (NN) have become of paramount importance in modern technology and science due to their ability to model and solve complex, non-linear problems that are difficult or impossible for traditional algorithms. These networks are capable of learning complex hierarchies of features, making them ideal for identifying patterns in a broad sense. That variability allows recognizing objects in real-time, adapting to the new scenarios and taking into account the complexity of the context. Neural networks are irreplaceable in tasks involving text, language translation, and speech recognition, dealing with visual data

and analysing medical data for alarming patterns for disease detection (Park and Han (2018)). Furthermore, NN paved the way for the development of autonomous driving, being able to process vast amounts of data from cameras, LIDAR, radar, and other sensors in real-time to make critical driving decisions. The non-linear nature of driving scenarios, involving unpredictable human behavior and environmental factors, makes neural networks the best solution for this high-stakes application. The ability to make the predictions makes them highly effective in areas like recommendation systems, stock market prediction, risk assessment, and algorithmic trading.

At the core of a neural network's functionality is a series of **Matrix-Vector Multiplications (MVM)** that occur within its layers (Shen *et al.* (2017)). A neural network consists of interconnected nodes (or neurons) organized into layers: an input layer, one or more hidden layers, and an output layer. Each connection between neurons carries a weight, and each neuron applies an activation function to determine if it should "fire." When data (in the form of vectors) is fed into the network, it is processed by the neurons in each layer through matrix-vector multiplications. Specifically, the input vector is multiplied by a weight matrix in each layer, and the resulting vector is passed through an activation function, which introduces non-linearity into the model. This process of matrix multiplication and activation continues as data flows through the network's layers, allowing the model to capture complex relationships in the input data. Training a neural network involves adjusting the weights in these matrices through a process called backpropagation, where the network learns by minimizing a loss function based on the difference between its predictions and the actual outcomes. This iterative process involves gradient descent to optimize the weights, ensuring that the model improves its accuracy over time. Given their reliance on MVM, NN scale well with parallel computing systems, which can handle large matrix operations efficiently.

The photonic platform provide an excellent solution for optimising MVM

with regards to energy efficiency and computation speed (Xu *et al.* (2023), . Brückerhoff-Plückelmann *et al.* (2022)). In optical domain, the modulation of the input vector in form of a broadband signal is done in a **crossbar array** (example in Fig.1.1). The crossbar array structure consists of rows and columns of optical waveguides, with the intersection points representing elements of the matrix. The input vector is encoded into the spectral intensity of an optical signal that travels through the rows. The matrix elements manipulate are represented by intensity or phase actuators, which modulate the properties of propagating light. The signals from each column are summed using the inherent properties of light (such as interference or power summation of incoherent light). This process occurs simultaneously for all elements, achieving a high degree of parallelism. After demultiplexing output signal can be transmitted into next layer of NN or resolved directly. The key factors for scalability of crossbar arrays are the losses in the passive elements and effectiveness of WDM.

### 1.2.2 Phase change materials

The essential elements of cross-bar arrays for optical domain MVM are the actuators in intersections. With them being genuinely weights of the matrix, their stability in terms of maintaining state and precision of the impact made on propagating signal are the pivotal factors of long-term matrix functioning. Signal manipulation is realised in modulating of different properties of light, like phase, intensity, polarization etc, and the actuators are driven by different physical mechanisms.

The promising candidate for this role are **Phase Change Materials (PCM)** (Wuttig *et al.* (2017), Abdollahramezani *et al.* (2020), Lankhorst (2005) and others). Having several meta-stable states (phases), PCM can exist under the same condition and expose different physical properties. Their phase can be manipulated, which provide their application as adjustable tunable signal modulators.

Preserving the state after switching, PCM embody the **non-volatile** passive elements, which can be introduced onto schemes for optical computing and data storage (Karpov *et al.* (2010)). Once encoded the matrix weights into PCM crossbar array, the enormous number of repetitive cycles of low-loss passive MVM are accessed.

To better represent the PCM as a signal modulator, let's consider some reported examples of MVM chips architectures, including PCM. Some of them are based on the coupling of the light in an alongside structure, resulting in the reducing of the propagating signal. The schematic image is given in Fig.1.1 There the waveguides are put alongside the crossbar arrays intersections. As a result of near field coupling, the output light signal is modulated with the losses in the alongside structure. Manipulating extinction coefficient of such a structure, one can attenuate the propagating signal, which corresponds to non-linear activation function of a node. Another structure can be realised with Ring Resonators (RR) in the intersections (Fig.1.1). As the RR geometry is tuned for the coupling of a specific spectral component only, slight change of the properties of the ring shifts the resonance, affecting the coupling and therefore modulating the signal propagating further through the array. For coupling manipulation one can change the Q-factor of the ring, or shift the peak via changing the effective refractive index. For programmability both architectures require a cell with manipulated complex refractive index, which can be realised by PCM.

**Non-volatile memory**

As it was described in papers Parra *et al.* (2021) and others, on-chip nonvolatile photonic memory would be a revolution in optoelectronic computing, reducing power consumption and accessing the multi-channel operations. Multi-level photonic memories with random access would allow for leveraging even greater computational capability with opening the multi-bit operation regime (Ríos Ocampo *et al.* (2015)). The important parameters, addressed in the area

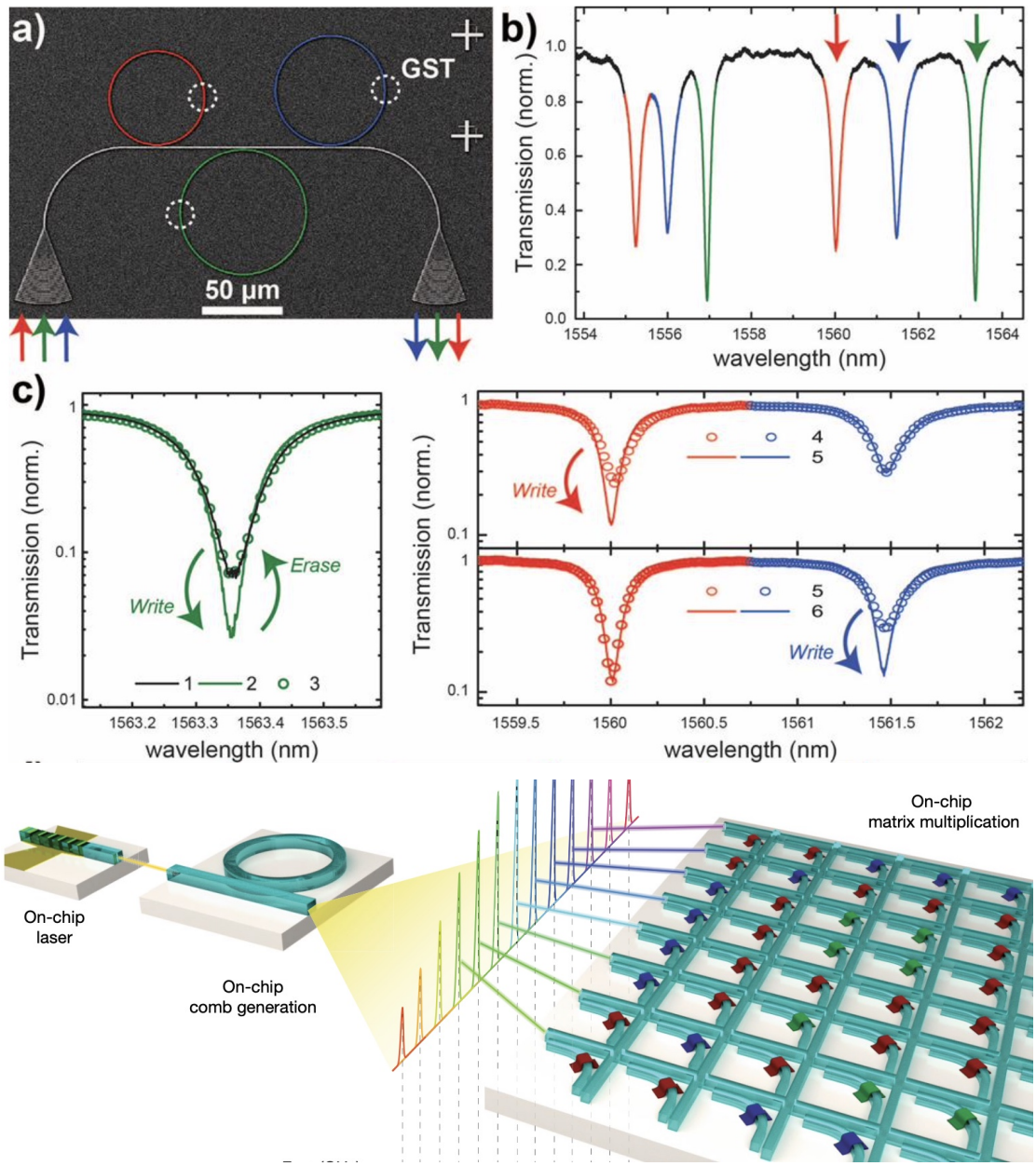


Figure 1.1: Top figure: Microringresonators for multi-wavelength signal modulation. From Ríos Ocampo *et al.* (2015). a-b) Three propagating channels, signal is modulated with nearfield coupling to RR. c) Selective signal modulation with local GST switching. Bottom figure: The crossbar array with PCM weighing elements on the intersections for MVM. From Feldmann *et al.* (2021)

of research and development of PCM, are robustness in terms of reproducible switching cycles, stability in terms of preserving the state between the cycles for divine non-volatility, and the switching speed rate. The ability to maintain the set properties lies down in the stability of the states. PCM mostly have 2 stable states, which correspond to the physical representation of binary memory. Nevertheless, the intermediate metastable states can be utilised, given precise setting and taking into account the slow thermal drift towards stability. The previous boom of the PCM usage was implementation of long term optical memory in DVDs. The local optical properties (namely reflectivity) of PCM change allows using switching for optical information encoding. Bit sequence is encoded into reflective ("1") crystalline and non-reflective ("0") amorphous states. The segments are read out with the scanning laser beam, the choice of which varied from one technique to other. The functionality region of PCM is covering the blue part of visible spectra, which was the advantage for Blu-Ray. The ability to form very localised amorphous and crystalline regions and using short-wavelength scanning laser were the keys for ultra-high data density, which allowed encoding movies in high quality. Once written and put under reasonable conditions, PCM preserve their states for decades, which made them a perfect choice for this technique and encouraged a big boost of their investigation. With the appearance of streaming platforms and digital HDD storages the era of Blue-Ray ended, but the investigation of PCM wasn't stopped.

**Re-writability**

Phase switch is an inherent capability of PCM, the mechanism of which is robust and does not lead to the material degradation (Mohseni and Novin (2023)). The observation of the physical processes, taking place during switching, will be given later, what is worth mentioning here is that it is heat-driven. The localisation of heating mechanisms define the efficiency of data encoding. The advancement in field of laser physics allowed to put reading and writing onto the

same laser platform. In DVD, CD and Blu-Ray the high power laser pulses are used for writing, while the low-power laser scanning is used for reading. The electrically driven state switch is utilised in random access memory storages, where both writing and reading are mediated with electric current. The drastic contrast between conductivity of the states realises the two-level bit structure, while the localised heater allows rapid state change. The development of PCM enhanced its ability to withstand the stress attributing to switching process, such as mechanical tension, oxidation rates etc. Such durable materials can undertake thousands of write/erase cycles, preserving its full functionality. Furthermore, the switching in PCM is happening on the microseconds scale, which push the writing rate to Mbps. For example, adjusting the laser properties for tunable switching, Blu-Ray technology allows push writing rate to 216 Mbps, which corresponds to 27 Mb/s.

**GST**

The techniques, mentioned in previous subsection, are operated on the chalcogenide-based PCM, so-called chalcogenide glass. The primary choice material is Germanium - Antimony - Telluride, $Ge_2Sb_2Te_5$ (GST), which is valued for the switching speed and prominent contrast in electrical and optical properties (Abdollahramezani *et al.* (2020)). The amorhpous GST exposes no order in its structure. It corresponds to high optical transmission, low reflectance, high electron scattering and electrical resistivity. Crystallised GST is organised into face-centred cubic lattice, which has drastically different physical behaviour. The crystall plates are light reflecting, which is recognised as "1" in scanning systems. The higher order enhances the charge movement, therefore the conductivity of this state is significantly bigger, which also correspond to "1" in an electrical read-out. Such a drastic difference allows the realization of intermediate states, which is a foundation for a multi-level memory. The state differentiation can be observed down to nanoscale cell size, which is a key factor for miniaturisation of the de-

vices and increasing packaging density.

## 1.3 Research objectives

The novel materials are an essential source of advancement in area of photonics in general and optoelectronics especially. Their development and evaluation is being performed in the laboratory conditions, where the properties of material as a whole are examined. For example, investigations of GST mostly report the properties of thin films, like sheet resistance or transmission measurements, whereas, going to the microscale, more and more physical mechanisms start to play a role. Talking about crystal structures, layers of 10nm thickness are almost falling to the monolayer category, which highlights the difference from the bulk structure. On that scale, atomic interactions with the surrounding impact the physical properties of the material greatly, which put a clear demand on the comprehensive description of its effective properties. Integrated in a structure, PCM interacts with the underlying materials, is exposed to the ambient atmosphere, acquire some manufacture defects and undergoes post-treatment procedures. Each of these steps contribute to the overall difference of the material physical response. As long as the crystallisation dynamic in nanolayers and bulk structures are a big unrevealed topic, the behaviour of the structures as a whole needs to be evaluated by experimental means.

In the context of optical properties of GST, the phase change affects mostly the imaginary part of the refractive index of the material, which changes the losses in a PCM-loaded structure and leads to the attenuation of the propagating signal. The straightforward method of a device evaluation are the direct transmission measurements. That method already allows differentiating between intermediate GST states and drawing conclusions about switching processes. Nevertheless, direct measurements are affected by other sources of losses, which are difficult to detect and eliminate, for example, insertion losses due to mis-

alignment and other. Another method, which relies rather on relative than absolute measurements, is **interferometry**. This method promises to be more accurate and provide more info about the structural optical properties, giving an insight into the change of complex effective refractive index.

The aim of this project is evaluating the performance of the GST-loaded structure on a photonic chip platform, comparing transmission measurements with interferometric. This project is inspired by the article by Faneca Ruedas *et al.* (2020), taking the research from O-band into C-band, where the state difference is reported to be even bigger. The PCM cell switching effect will be evaluated by two different means, delivering comprehensive information about the properties of integrated GST.

# CHAPTER 2

# Materials and methods

## 2.1 GST treatment

Initially GST was deposited on a chip, using Electron Beam Physical Evaporation. The uniformity of deposition was secured for the patch sized of 3-7x2 μm, used in this work. Deposited from vapour phase, the molecules in GST are located randomly, therefore the material in "as-deposited" state is amorphous. As it was mentioned before, the phase transition in GST is heat-driven, while the devices are operated under normal conditions in ambient atmosphere. To prevent oxidation, the $Al_2O_3$ coating was deposited as well, resulting in mitigation degradation effects.

To get the effective signal reduction, the PCM cell need to be *switched* — the structure of GST should undergo transition to get higher order. Crystallisation from the amorphous state starts with heating the material up to the glass transition temperature $T_g$. The crystallities of rocksalt (cubic) structure start to form, making crystallization paths along the temperature gradient. Rocksalt structure is an intermediate metastable state, as it include a lot of vacancies and is not energy favourable. However, cooled down in that phase, GST would expose partial optical transmission attenuation, and this intermediate state can be held for the considerably long time (Mohseni and Novin (2023)). This mechanism paves a way to multi-leveled optical memory systems. Left heated above $T_g$ for a longer time, GST acquire spinnel crystall structure, in which Ge atom has stable tetrahedral coordination (in comparison with octahedral configuration in rocksalt structure). This state provides the most attenuation of the optical signal and can be defined as *completely switched*. Switching GST back to the amorphous state

goes under converse conditions — the material should be heated up to melting temperature $T_m > T_g$ and then rapidly cooled down, yielding disordered quasi-amorphous structure by the melt quenching.

With regard to these underlying physical mechanisms, for crystallisation of GST prolonged ($\sim 10^{-7}$s ) heating under moderate peak power is needed, while for backwards transition short ($\sim 10^{-9}$s) and high-energy shots are needed. Those conclusions are presented in Fig.2.1b.

### 2.1.1 Switching techniques

The structural properties of the materials after switching depends greatly on the treatment methods, therefore the switching methods and parameters are explicitly specified in PCM investigation researches. Here the brief overview of switching techniques is given, with highlight on the methods used on this work.

The most straigntforward method of crystallising GST is its external heating. Using annealing, long heating on a hot plate with prolonged subsequent cooling, the proper crystalline *hcp* structure is acquired. GST starts to change phase, heated up to $240^oC$ or more. The uniform heat distribution and long following cooling time allow atoms to align itself into an energy-favourable stable crystalline structure. This state provide the biggest electrical conductivity and optical attenuation.

However, this method, being helpful for the material investigation, cannot be used for agile switching. Furthermore, it cannot be used for GST amorphisation. To control switching, which in our case is directly connected with signal modulation, high speed on-chip device switching is needed. It can be realised in form of directly embedded heaters, temperature of which depends on the applied voltage. For example, graphene heaters can be heated up and cooled down very fast, which allows high-speed modulation on the µs scale (Ríos *et al.* (2021)). Another approach to it is applying voltage directly to GST

cell (Karpov *et al.* (2010)). Due to partial conductivity via crystallisation paths, the current is flowing through the structure, dissipating and Joule heating the material around. This method is less controllable, as the conductivity rises with rise of the crystalline fraction and reduces the Joule heat flow 2.1. In this case heating condition alters and further crystallisation slows down. Nevertheless, both methods are widely used for modulating electrical signals via conductivity changes.

$$\frac{dP}{dV} = \vec{J} \cdot \vec{E} = \vec{J} \cdot \vec{J}\frac{1}{\sigma} = J^2\sigma \tag{2.1}$$

where $\vec{J}$ is current density, $\vec{E} = \frac{1}{\sigma}\vec{J}$ is the electric field and $\sigma$ is conductivity.

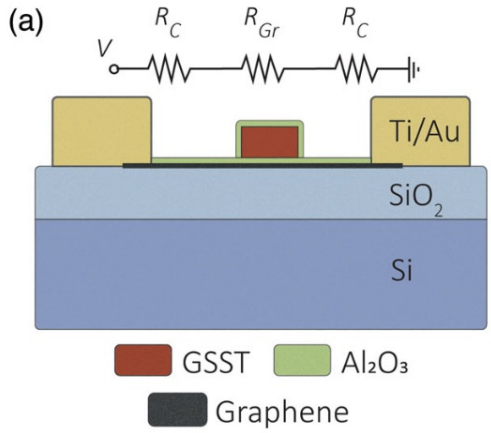


(a) Sketch of the transversal section of the device comprising a graphene microheater and a 50 nm GSST cell. The writing (heating) and readout electrical pulses are delivered through the same channel. Reprinted from Ríos *et al.* (2021)

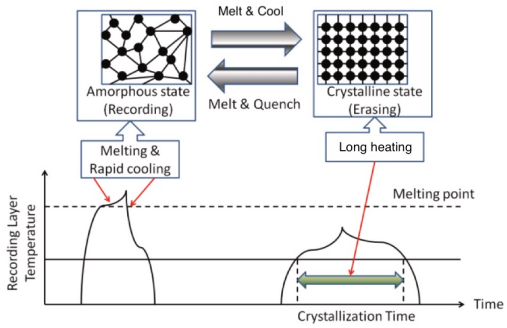


(b) Manipulation of GST state via heating pulses. Independently of specific method, the long pulses of moderate amplitude are used for organising the crystall structure, short and powerful pulses are used for meling and quenching. Reprinted from Mohseni and Novin (2023).

Figure 2.1: GST switching as a result of heating.

In case of optical modulation of signal on the photonic platform, any metallic wiring is generally non-favourable. These structures, being embedded, introduce additional losses, which significantly hinders the scaling and diminish the energy efficiency. Thus, optical switching via laser induced material heating is preferable and is introduced into usage. In that case the intensity and time-form of switching pulses define the conditions for phase switching and govern

the effective signal modulation.

The most effective way for operating packaged chips would be in-plane laser switching, where the switching laser pulses are brought to the PCM structures directly through waveguides. Being absorbed, switching pulse heats the material and changes its structure, which results in the modulation of the working signal on different wavelength. This method is especially applicable for spiking neural networks functioning, which is not covered in bounds of this particular work.

In this work out of plane laser switching is used, as it gives full control of the all parameters of interest: pulse length, repetition rate (which is effectively moderate the cooling time), the peak and average powers, intensity distribution, and additionally provide more geometrically uniform heating of the PCM cell.

### 2.1.2 Experimental setup

For this experiment a *MaiTai* optical setup (Fig. 2.2) was designed. Its primary part is a pulsed ultrafast titanium-sapphire laser, operating at a wavelength of $\lambda$=800nm, boasting a repetition rate of $\nu$=80MHz and a pulse duration of $\Delta$t=15fp. The laser output is directed into a pulse picker employing an Acousto-optic modulator (AOM), enabling the selection of a designated number of pulses to effectively reduce the repetition rate to $\nu$=8MHz. The initially y-polarised beam is propagated through rotatable polarizer for power flux modulation. After collimation the beam undergoes two successive splits by a 50:50 and 90:10 beamsplitters. The first beamsplitter delivers 50% of the original to a power meter for continuous monitoring of the system's input power. Approximately 45% of the initial laser power reaches the galvo, a scanning mirror system. The galvo mirrors direct the beam into a microscope objective, which focuses it down to the spot size of $d \approx 3.5m$. The sample is mounted on a micron-stage system, facilitating precise movements along the x, y, and z axes.

Galvo mirrors' deflection angles allow to scan across the sample along x- and y-axis, while relative distance between the objective and the sample is controlled with vertical stage movements. The intensity distribution in the laser spot size is governed by fundamental diffraction laws and can be described with Point Spread Function. Exposing structure to the pulses multiple time, the rather uniform coverage is achieved, and heating process is initialised across all the PCM cell. The effectiveness of the switching process on a device hardly can be defined directly while laser exposure. The evaluation methods, which would be discussed later, are involving other techniques. However, the MaiTai setup includes imaging system: signal from a white light source is channeled through a Koehler illumination setup before being introduced into the beam path via the 90:10 beamsplitter and illuminate the chip. The reflected white light is then back propagated to the CCD-camera to produce a 50x magnified image of the chip. Observing the results of laser exposure on thin GST films, one can notice change of the material reflectivity at places where it was switched: amorphous regions seem darker than partially crystallised one.

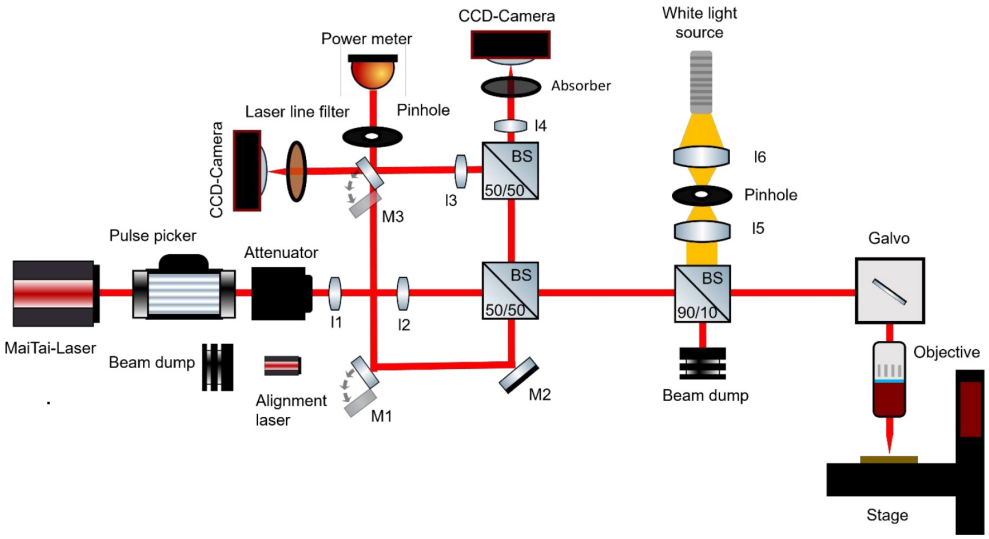


Figure 2.2: *MaiTai* laser setup

## 2.2 Evaluation methods

Phase transition in PCM change the properties of the material and the performance of the device in general. Evaluation of the effectiveness of switching is needed for choosing optimal parameters for device operation. Namely, in case under investigation, the parameters of laser pulses for different switching levels should be defined. The evaluation methods can be classified as invasive and non-invasive. Invasive investigation provides more broad information on the material structure, non specifying directly how it affects the physical properties, while non-invasive methods are based on measurements of device performance and give only vague idea about the structural changes themselves. Here some methods are described with a highlight on ones, used in this particular work.

### 2.2.1 SEM

Scanning Electron Microscopy (SEM) is an imaging method, operating electron beam instead of light. SEM image is formed from the reflected and scattered electrons. Electrons are interacting with the atoms on the surface of the exposed sample, therefore in case of layered structures SEM provides information about shallow area on the top part. The mechanisms of electron-atom interaction differ, providing information about distribution of the atomic masses, electron density, general density, crystall structure etc. Scattering of low energy electron beam provide the information about the materials and its local changes. The energy of backscattered electrons depends on the atomic number of the scatterer, therefore this imaging method shows changes in the observed material on terms of overall Z-value by the signal intensity (light and dark grey colour). Having more dense atom packaging, crystalline GST seems lighter in the pictures (Harmgarth *et al.* (2017)). In this work SEM of backscattered electrons was used for imaging the devices as a whole and for visualisation of switching

results.

### 2.2.2 Transmission measurements

For evaluating the effect, made by PCM switching, detailed information about material structure might be excessive. In this work, the optical performance is to be evaluated, therefore its direct measurements are obvious first choice.

As it was mentioned in 1.2, the property of interest in PCM-containing optical hardware is the effective attenuation of the signal in a structure, resulting in intensity modulation. To obtain it, measurements of transmission of a waveguide structure are used. In the scope of this work this measurements are done using a backloop structure (Fig. 2.3a). It operates in following manner: the input signal (continuous wave laser signal at the wavelength $\lambda = 1550nm$) is coupled into a $Si_3N_4$ waveguide via fiber array. Light is equally splitted in MMI and then propagated through the symmetrical waveguide arms structures. The GST patch is deposited on one arm. The signal is coupled back into fiber array via the same grating couplers, then 2 signals are registered on Photodetectors. The effective output of a measurement is transmission spectra of both pure and GST-loaded loops. The ratio of signals provide the information about the attenuation in the GST-loaded loop (Fig. 2.3b).

Such measurements are affected by some accompanying effects, for example misalignment of read out fiber array and subsequent shift of the grating coupler transmission window, minor defects in the loops, uneven intensity splitting in MMI, faulty grating couplers, dirt or dust on the surface etc. Some of them can be mitigated: effects of misalignment are cut out with measuring systematic error on the reference device (both loops without GST patch, Fig. 2.3b), dirt is washed off, the sensitivity of the diodes is equalised. However, all those effects significantly reduce reliability and precision of transmission measurements.

To represent the pipeline of the transmission measurements execution and

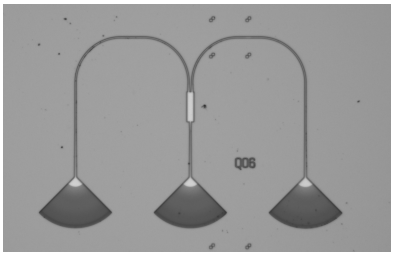


(a) Single Backloop structure. Markers point the location of a GST patch and are used for navigating during laser switching

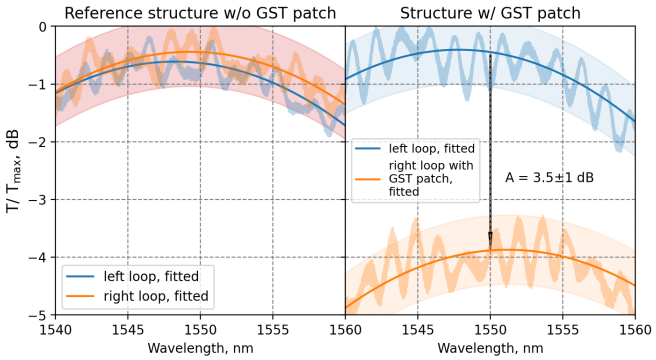


(b) Signal ratio, recorded from reference device (left), is used to eliminate of systematic misalignment error. Signal ratio in a device with a GST patch on it (right) yields the attenuation (A) in the structure.

Figure 2.3: Transmission measurement, accompanied with reference measurement of a symmetric structure without GST patch on it. Going below the limit of systematic error is hardly possible.

data processing, some formalism can be put. Firstly, the reference structure should be considered. Due to the symmetry of the structure, the transmission function (TF) $T^0(\lambda)$ is the same for both arms. The light is coupled in and out via grating couplers. In spite of structural symmetry, the TF of those is highly affected by the alignment of the fiber array. Attributing $T^0_{CC}(\lambda), T^0_1(\lambda), T^0_2(\lambda)$ to the TF of central, right and left grating couplers accordingly, given the intensity of input light as $I_{in}(\lambda)$, we could express the resulting read out from the reference structure as

$$I^0_i(\lambda) = T^0_i(\lambda)T^0(\lambda)T^0_{CC}(\lambda)I_{in}(\lambda), \qquad \frac{T^0_1(\lambda)}{T^0_2(\lambda)} = \frac{I^0_1(\lambda)}{I^0_2(\lambda)} \tag{2.2}$$

Moving from reference device to the GST loaded structure, the transmission of the right arm is affected by $T_{GST}(\lambda, l)$, where $l$ stays for the length of GST patch. This function is our main focus, and can be extracted from the intensity

measurements $I_i$, applying the ratio from the reference measurements 2.2.

$$
\begin{aligned}
I_1 =& T_1^0(\lambda) T_{GST}(\lambda, l) T^0(\lambda) T_{CC}^0(\lambda) I_{in}(\lambda), \\
I_2 =& T_2^0(\lambda) T^0(\lambda) T_{CC}^0(\lambda) I_{in}(\lambda), \\
T_{GST}(\lambda, \mathrm{l}) =& \frac{T_1^0(\lambda) T_{GST}(\lambda, l) T^0(\lambda) T_{CC}^0(\lambda) I_{in}(\lambda) \cdot \frac{T_0^2(\lambda)}{T_0^1(\lambda)}}{T_2^0(\lambda) T^0(\lambda) T_{CC}^0(\lambda) I_{in}(\lambda)} = \\
& \frac{I_1(\lambda, \mathrm{l})}{I_2(\lambda)} \cdot \frac{T_0^2(\lambda)}{T_0^1(\lambda)} = \frac{I_1(\lambda, \mathrm{l})}{I_2(\lambda)} \cdot \frac{I_2^0(\lambda)}{I_1^0(\lambda)}
\end{aligned}
\tag{2.3}
$$

### 2.2.3 Mach Zender Interferometer

Interferometry provides comprehensive information about the optical properties of the DUT, allowing to evaluate the complex refractive index and describe not only attenuation, but also the propagation constant. Real part of the effective refractive index is not of paramount importance for application in weighed crossbar arrays, but it plays a role in scaling the hardware sizes, multistage signal processing and pushing computation rates. Furthermore, the information about imaginary part of the effective refractive index, which also can be extracted from these measurements, has high precision

To explicitly show the interconnection between interferometric pattern and complex refractive index, a theoretical model of MZI should be considered. Generally, MZI can be factorized into 2 MMI's and 2 arms of lengths $L_1$ and $L_2$, providing phase shift (and attenuation) according to their length and effective refractive index. As the propagating fields have the $\pi$-shift at the outputs of 1x2 MMI (Soldano and Pennings (1995)), in 2.4 MMIs can be expressed as unitary matrixes applied to single input and observed for single output $a_{\text{out}}$ (the time dependencies are omitted throughout the matrix derivations) :

$$\begin{pmatrix} a_{\text{out},1} \\ a_{\text{out},2} \end{pmatrix} = \frac{1}{2} \begin{pmatrix} 1 & j \\ j & 1 \end{pmatrix} \begin{pmatrix} e^{\frac{2\pi j}{\lambda}(L_1 n_{WG} + l_{GST}\overline{n_{GST}})} & 0 \\ 0 & e^{\frac{2\pi j}{\lambda} L_2 n_{WG}} \end{pmatrix} \begin{pmatrix} 1 & j \\ j & 1 \end{pmatrix} \begin{pmatrix} a_{\text{in},1} \\ 0 \end{pmatrix} \tag{2.4}$$

$$\begin{pmatrix} a_{\text{out},1} \\ a_{\text{out},2} \end{pmatrix} = \frac{1}{2} e^{\frac{2\pi j}{\lambda} L_2 n_{WG}} \begin{pmatrix} 1 & j \\ j & 1 \end{pmatrix} \begin{pmatrix} e^{\frac{2\pi j}{\lambda}(l_{GST}\overline{n_{GST}} + \Delta L n_{WG})} & 0 \\ 0 & 1 \end{pmatrix} \begin{pmatrix} 1 & j \\ j & 1 \end{pmatrix} \begin{pmatrix} a_{\text{in},1} \\ 0 \end{pmatrix} \tag{2.5}$$

$$\begin{pmatrix} a_{\text{out},1} \\ a_{\text{out},2} \end{pmatrix} = \frac{1}{2} e^{\frac{2\pi j}{\lambda} L_2 n_{WG}} \begin{pmatrix} 1 & j \\ j & 1 \end{pmatrix} \begin{pmatrix} e^{j\varphi} & j e^{j\varphi} \\ j & 1 \end{pmatrix} \begin{pmatrix} a_{\text{in},1} \\ 0 \end{pmatrix} \tag{2.6}$$

$$\begin{pmatrix} a_{\text{out},1} \\ a_{\text{out},2} \end{pmatrix} = \frac{1}{2} e^{\frac{2\pi j}{\lambda} L_2 n_{WG}} \begin{pmatrix} e^{j\varphi} - 1 & j(e^{j\varphi} + 1) \\ j(e^{j\varphi} + 1) & -(e^{j\varphi} - 1) \end{pmatrix} \begin{pmatrix} a_{\text{in},1} \\ 0 \end{pmatrix} = \frac{a_{\text{in},1}}{2} e^{\frac{2\pi j}{\lambda} L_2 n_{WG}} \begin{pmatrix} e^{j\varphi} - 1 \\ j(e^{j\varphi} + 1) \end{pmatrix} \tag{2.7}$$

$$a_{\text{out},1} = \frac{a_{\text{in},1}}{2} e^{\frac{2\pi j}{\lambda} L_2 n_{WG}} (e^{j\varphi} - 1), \quad \text{where}$$

$$\varphi = \frac{2\pi}{\lambda}(l\overline{n_{GST}} + \Delta L n_{WG}),$$

$$\Delta L = L_1 - L_2, \quad \overline{n_{GST}} = n + j\kappa$$

$$j\varphi = \frac{2\pi j}{\lambda}(ln + jl\kappa + \Delta L n_{WG}) = \frac{2\pi j}{\lambda}(ln + \Delta L n_{WG}) - \frac{2\pi\kappa}{\lambda} l$$

$$j\varphi = \beta + j\alpha, \quad \alpha, \beta \in \mathbb{R},$$

$$\alpha = \alpha(\lambda, l, L) = \frac{2\pi}{\lambda}(ln + \Delta L n_{WG})$$

$$\beta = \beta(\lambda, l) = \frac{2\pi\kappa}{\lambda} l$$

Proceeding to the real observable, the recorded data is output power spectrum $P_{out}(\lambda)$, which can be functionally decomposed into constant level and interferometric part. The spectral transmission depends on the GST patch length and the arm length difference as following:

$$P_{out} = a_{\text{out},1} a^*_{\text{out},1} = \frac{a_{\text{in},1} a^*_{\text{in},1}}{4} (e^{j\varphi} - 1)(e^{j\varphi} - 1)^*$$
$$T = \frac{P_{out}}{P_{in}} = \frac{1}{4}(e^{j\varphi} - 1)(e^{j\varphi} - 1)^* = \frac{1}{4}(e^{-\beta} e^{j\alpha} - 1)(e^{-\beta} e^{-j\alpha} - 1)$$

$$T(\lambda, l, L) = \underbrace{\frac{1}{4}(e^{-2\beta} + 1)}_{\text{constant level}} - \underbrace{\frac{1}{2} e^{-\beta} \cos\alpha}_{\text{interferometric part}} \tag{2.8}$$

To express the quantity of interest $\overline{n_{eff}} = n + j\kappa$, the local variables $\alpha$ and $\beta$ need to be evaluated with the help of parameters of the observable interferometric pattern, namely visibility ($v$, 2.9), period (or FSR, $\Delta\nu$, 2.11) or shift of the interferometric peaks ($\Delta\Lambda$, 2.12) after switching GST from amorphous state to crystallized (with the real part of the effective refractive index read as $n_1$ and $n_2$ accordingly). Visibility can be put into the more convenient values in the manner 2.10. From the simulation, result of which will be presented later in Chapter 3.1, $n_1 < n_2$, therefore $\Delta n = n_2 - n_1 > 0$. At the same time, the effective refractive index of the structure loaded with thin amorhpous GST layer is very close to one of the simple waveguide ($n_1 \approx n_{WG}$), which will be used for the simplification of the derivations in 2.12.

$$v = \frac{P_{max} - P_{min}}{P_{max} + P_{min}} = \frac{P|_{\cos\alpha=-1} - P|_{\cos\alpha=1}}{P|_{\cos\alpha=-1} + P|_{\cos\alpha=1}} = \frac{2e^{-\beta}}{e^{-2\beta} + 1} \tag{2.9}$$

$$\begin{aligned} \mathrm{ER} = P_{max}[dB] - P_{min}[dB] =& 10log_{10}(\frac{P_{max}}{P_min}) \rightarrow \frac{P_{max}}{P_{min}} = 10^{\frac{\mathrm{ER}}{10}} \\ v = \frac{P_{max} - P_{min}}{P_{max} + P_{min}} =& \frac{P_{max}/P_{min} - 1}{P_{max}/P_{min} + 1} = \frac{10^{\frac{\mathrm{ER}}{10}} - 1}{10^{\frac{\mathrm{ER}}{10}} + 1} \end{aligned} \tag{2.10}$$

$$\begin{aligned} T|_\nu = T|_{\nu+\Delta\nu} \quad \rightarrow \quad \cos\alpha|_\nu = \cos\alpha|_{\nu+\Delta\nu}, \\ \alpha = \frac{2\pi}{\lambda}(ln + \Delta Ln_{WG}) = \frac{2\pi c}{\nu}(ln + \Delta Ln_{WG}) = 2\pi \cdot m, m \in \mathbb{Z} \\ \Delta\nu = \frac{c}{ln + \Delta Ln_{WG}} \end{aligned} \tag{2.11}$$

$$\begin{aligned} \frac{ln_1 + \Delta Ln_{WG}}{\lambda_1} &= \frac{ln_2 + \Delta Ln_{WG}}{\lambda_1 + \Delta\Lambda} \\ (ln_1 + \Delta Ln_{WG})(1 + \frac{\Delta\Lambda}{\lambda_1}) &= ln_2 + \Delta Ln_{WG} \\ (ln_1 + \Delta Ln_{WG}) \cdot \frac{\Delta\Lambda}{\lambda_1} &= l\Delta n \\ \Delta\Lambda &\approx \lambda_1 \cdot \frac{l}{l + \Delta L}\frac{\Delta n}{n_{WG}} \end{aligned} \tag{2.12}$$

Although deriving the exact numbers needs meticulous treatment, the main conclusion must be taken into further measurement evaluation:

- from 2.9, visibility of interferometric pattern decreases with increase of attenuation in one of the MZI arms. In conventional logarithmic scale (dB) it manifests as reduction of Extinction Ratio (ER).
- from 2.11, FSR is decreasing with the
  1. increase of the real part of effective refractive index of GST-loaded structure
  2. increase of the length of GST patch
  3. increase of arm length difference
- from 2.12, the red shift of the peaks is observed with the increasing of the real part of effective refractive index. Furthermore, the less is the MZI arm difference, the more pronounced the shift is.

# CHAPTER 3

# Experimental part

## 3.1 Modelling

Preliminary modelling is a pivotal part of the manufacture of any optoelectronic device. It allows to choose the optimal parameters for required performance, saving time and manufacture resources. However, the flawless theoretical model cannot be directly applied to a real device, affected by manufacture and post-treatment processes. Nevertheless, adjusting simulation parameters, such as refractive indexes, real geometry etc, the better results can be acquired, providing refinement of estimation picture. In this Section the modelling process is described and the estimation of the interferometric pattern is set.

### 3.1.1 FDTD modelling of the field propagation

The initial step is the visualization of field distribution in the structure of interest and optimisation of the geometrical parameters. The most prominent computational method for dynamically changing fields is **F**inite-**D**ifference **T**ime-**D**omain. It is widely used in modelling optical devices down to nano-scale, and in the scope of this work it is utilised via the commercial Ansys Lumerical Software. The optimal parameters for the $Si_3N_4$ platform were derived within previous works, therefore the task was the optimisation of the GST patch geometry and acquiring the estimation for the effective refractive index of the structures.

The structure of interest is the straight piece of $Si_3N_4$ waveguide with a thin patch of GST on top of it. The schematic of the structure is given in the

Fig.3.1. The spectral refractive index for each material was acquired from the available literature and lab measurements. This fact as itself already puts an error in the result estimation. The refractive index measurements for GST are done via transmission measurements for *thin films*. In this cases, as-deposited GST is taken as fully amorphous, and annealed GST is fully crystallised. However, during switching, the heat driven crystal formation and quenching amorphisation result in structures, which are in between of those stable states (Wang *et al.* (2020)). The crystal structure and properties of the intermediate states differ, which is favourable with the regard to creation of multi-level memory, but puts a challenge for modelling it and predicting the performance. Furthermore, the nano-layer of GST is highly affected by the interfacial interaction with the waveguide and coating materials, which make the optical response on the atomic level to be different to one in the bulk structures. Nevertheless, simulation was essential to justify the geometry choice.

After preliminary mesh convergence test, the field distribution was observed in the device with GST patch in crystalline and amorphous states. The remarkable feature is the fact, that the thin layer of the amorphous GST does not significantly change the field distribution comparing to the field in a pure $Si_3N_4$ waveguide (Fig. 3.2b). At the same time, crystalline GST is more optical dense, which change the field distribution and leads to bigger confinement (bigger $\mathbb{R}(\overline{n_{eff}})$). The propagating field in this case tend to locate near the $Si_3N_4$-GST interface and protrude into GST (Fig.3.2c). Due to the remarkable extinction coefficient of the crystalline GST this led to the excessive attenuation. Simulation allowed to choose the trade-off between the confinement and the attenuation to be at the GST layer thickness of 20 nm, which was considered in design of MZI chip. Also, this thickness correlates with the estimated depth of the laser pulse switching effect. Note, that transmission measurements were performed using the already existing bakcloop chip with thinner GST, therefore separate simulation was done for comparison to the effective attenuation in these structures

(Fig.3.3b).

### 3.1.2 Interferometric pattern estimation

The theoretical description of an MZI model, 2.2.3, allows us to derive quantities of interest from the experiment. Nevertheless, for the sake of completeness it is reasonable to compare it to the results of the simulation and make some refinements on the model or on the simulation parameters itself. For the estimation of MZI response, the dispersion of effective refractive index was acquired (Fig. 3.3a). Using it, the MZI model was evaluated using Python3 framework. Based on the 2.8, the spectral transmission was plotted (Fig. 3.11). With variation of the arm difference $\Delta L$ the FSR $\Delta\nu$ changes significantly, which leads to more or less pronounced peak shift after *switching*, as it was assumed by 2.12. At the same time, varying the length of the attenuating GST patch $l$, the visibility of the interferometric pattern changes.

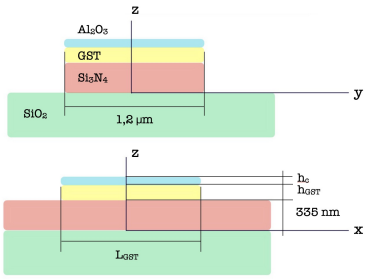


| Structure | Material | Backloop | MZI |
|---|---|---|---|
| Substrate | $SiO_2$ | 3.3 µm | 3.3 µm |
| Waveguide | $Si_3N_4$ | H:330 nm<br>W:1.2 µm | H:335 nm<br>W:1.2 µm |
| Patch | GST | H:12 nm<br>W:1.2 µm | H:20 nm<br>W:1.2 µm |
| Coating | $Al_2O_3$ | H:5 nm<br>W:1.2 µm | H:10 nm<br>W:1.2 µm |

Figure 3.1: Parameters of the modelled structures. The structures, used in backloop and interferometric chips are slightly different (MZI chip has thicker GST), as it was designed later, considering the previous experiments on backloops chips with thinner GST.

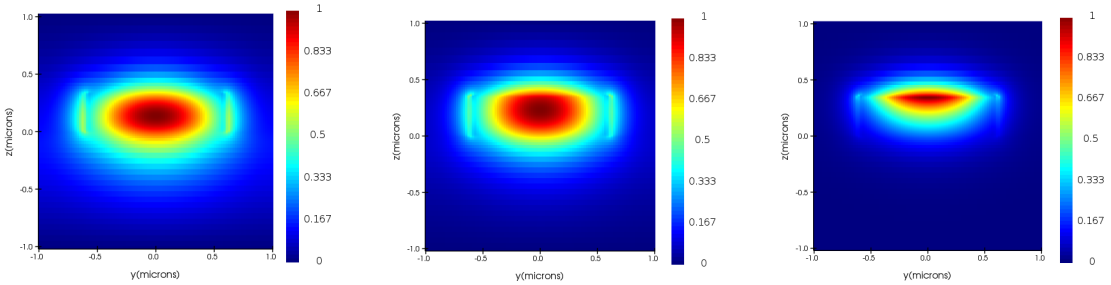


(a) Pure $Si_3N_4$ waveguide

(b) $Si_3N_4$ waveguide with **amorphous** GST on top

(c) $Si_3N_4$ waveguide with **fully crystalline** GST on top

Figure 3.2: The normalized power distribution in cross section of the structure of interest for fundamental $TE_{00}$ mode

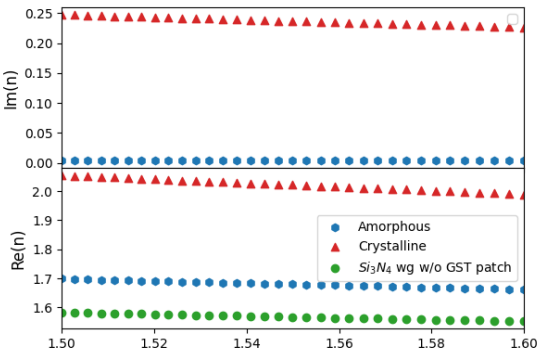


(a) Dispersion of the structure from Lumerical simulation (with pure material dispersion parameters)

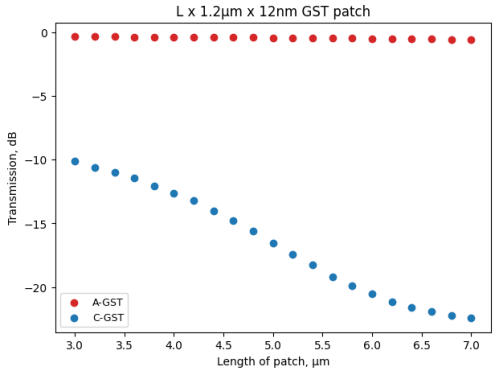


(b) The attenuation of the signal in a structure with fully crystallised GST on top

Figure 3.3: Optical constants estimation

## 3.2 On-chip MZI device

The important milestone in this work was the design of the chip layout. Aside from the experiment details that were chosen based on the simulation, the global parameters for other structures, such as grating couplers (GC), MMI's and waveguides need to be considered. Those parameters were chosen with according to previous experiments and optimisation procedures, carried out in the working group. The layout for the automatised manufacture was made in KLayout. The design of the experiment implied varying the difference of the MZI arms length and the length of the GST patch. The GC parameters were optimized for coupling of C-band signals, having the transmission window at 1530-1570nm with a peak at 1550nm. The coupling angle was chosen to be $8^o$. The couplers of MZI are at the same height, it allows to input and output signal using a single fiber array. This alignment implies arched form of MZI arms, which were modelled with symmetric Bezier curves. Usage of Bezier curves provide smooth conjunction with the straight segment of the MZI arch, which reduce scattering losses. The drawback of this approach was the difficulty to control the arm difference. It was made automatically during creating the layout and resulted in $(300 \div 1000)$ + 2 μm with a step of 100 μm. The 1x2 MMI were balanced. The GST patch was located on the straight segment of the longer MZI arm and surrounded with pointers. The length of the patch was varied from 3 to 7 μm with the step of 0.5. The thickness of GST was chosen based on simulation results from 3.1 to be 20 nm. GST was coated with 10 nm of $Al_2O_3$.

For optimal experiment evaluation a numerous test structures were included on the chip. Simple backloop structure of 2 grating couplers and a waveguide is used for alignment and acquiring of TF of grating couplers itself. The MZI of different arm length with **no GST patch** on it are put for evaluation of the systematic error of laser scanning (wavelength offset) and effects of having as-deposited GST patch itself.

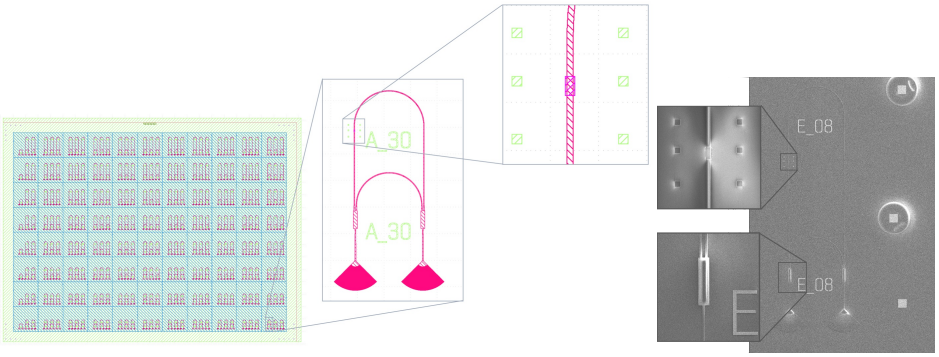


(a) Single device layout.

(b) SEM image of manufactured device

Figure 3.4: MZI chip design and manufacture

**Manufacture**

The photonic structures are designed using gdshelpers, an open-source Python framework for integrated circuit design. We use a material stack consisting of stoichiometric LPCVD $Si_3N_4$ films (330 nm) on a $SiO_2$ dielectric layer (3300 nm) with a silicon substrate and no cladding. The wafers are sourced from Rogue Valley Microdevices. Our process flow involves three main steps: writing gold markers, patterning the photonics, and patterning the phase-change material (GST).

For the gold markers, a positive photoresist (PMMA) from the AllResist AR-P 672 series is spin-coated and baked. The marker regions are exposed using a 100 kV electron beam lithography tool (Raith EBPG 5150). The chip is then developed in a solution of methyl isobutyl ketone (MIBK) and isopropyl alcohol (IPA). A stack of chromium (5 nm), gold (80 nm), and another chromium (5 nm) layers is deposited via physical vapor deposition (PVD), with chromium enhancing adhesion and protecting the gold surface. Finally, the resist is lifted off in acetone to reveal the markers, which are used for alignment in the subsequent steps.

For photonic patterning, we use a negative resist (AR-N 7520 series), spin-coated to a thickness of 350 nm. The waveguide regions are exposed with an electron beam using low currents and small step sizes for high precision. After developing the chip in Microposit MF-319, we etch the unexposed silicon nitride regions using a Reactive Ion Etching (RIE) tool with a $CHF_3$ and $O_2$ plasma. The resist is then stripped with oxygen plasma.

To pattern GST, we use a double layer resist consisting of MMA coploymer (AR 617 series) as a bottom layer and PMMA as a top layer. The resist is exposed where the phase-change material is required. After development, a 20 nm layer of GST is sputtered onto the chip, followed by a 10 nm layer of Alumina as a protective coating. Finally, the resist is lifted off using acetone.

## 3.3 PCM switching

Out of plane laser switching was done using the *MaiTai* setup, described earlier (2.1.2). The numerous parameters were to be optimised for acquiring accurate signal modulation via controllable switching. The initial parameter choice was based on the literature (Nevzorov *et al.* (2023), Ríos Ocampo *et al.* (2015) and other) and was adjusted to the setup specification. The operating wavelength of $\lambda = 780$ nm was chosen. Highly above the absorption edge for both crystalline and amorphous phases (0.5eV and 0.7eV accordingly, Pirovano *et al.* (2004)), this wavelength provides sufficient energy flux for quenching amorphisation via ultrashort pulses, corresponds to the absorption peaks of (partly) crystallised fractions and is generally well absorbed. The focal laser point was $d \propto 3.5m$, the laser repetition rate 8 MHz, the pulse duration 100 fs.

The parameters for variation were exposure time and the average power. For evaluation of the switching effect and choosing proper parameters the methods, described in 2.2, were used.

### 3.3.1 Microscopy

The basic noninvasive evaluation method is direct observation. As it was mentioned before, the phase change changes the reflectance of GST, which can be seen in optical microscope. This approach yielded to be sufficient for detection of amorphous, crystalline and burned states of GST on thin filma, although its contrast was relatively low. This method was prominent for quick automated parameter tests on thin GST films. There were still space for the improvement:

- as it was mentioned before, on nanometer scale properties of the material depend on the surroundings. The parameters, suitable for thin films, should be slightly adjusted when transferred to patch on a waveguide structure.
- the contrast of imaging was relatively low. Optical imaging was accompanied by SEM to evaluate different levels of switching, but it was hardly possible to say the state of small GST patch from SEM images.
- optical differences sometimes were not recognisable. For thicker structure, used in the loaded devices (20 nm GST, 10 nm alumnia), even long exposure to high power didn't lead to visible change, while, from general considerations, the phase change should have taken place.

To make the evaluation complete, further measurements via other methods were performed.

### 3.3.2 Transmission measurements

The most important parameter of a GST patch as an actuator is the contrast in optical properties between states. Therefore the transmission of a loaded waveguide was measured, using backloops, which were described switching in 2.2.2. The Figure of Merit was the peak transmission in the GST loaded loop normalised by the transmission in corresponding reference loop. Signal attenuation was related to the crystallisation process, restoration corresponded to quenching amorphisation. Average power was varied between 0.6–1 mW (which corresponded to 0.6–1 **W** peak power), the exposure time was varied $1e^{-3} \div 5e^{-2}$ s for

(a) Thin film of amorphous GST with crystallised regions, forming KIP logo.

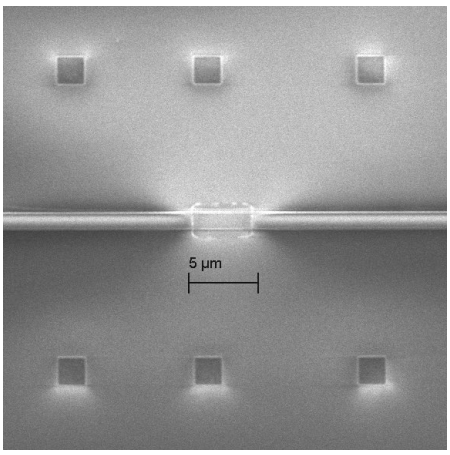


(b) SEM image of a GST-loaded waveguide. Thin GST layer is clearly seen, though its state cannot be defined.

Figure 3.5: Imaging of GST for switching evaluation.

crystallisation and $5e^{-5} \div 5e^{-4}$ s for re-amorphisation. The results are presented in the Fig.3.6 and Fig.3.7. Notwithstanding, the results of the transmission measurements were not accurate enough to make a resolution about preferable operating condition.

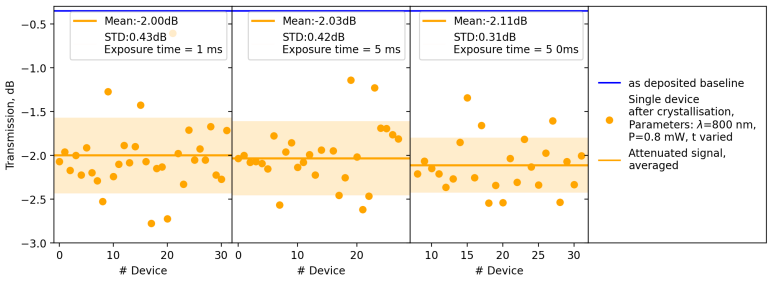


Figure 3.6: Attenuation of the input signal, measured at the peak of transmission window, after switching GST from as-deposited (amorphous) to partly crystalline state

### 3.3.3 Interferometric measurements

The more comprehensive results were expected from interferometry, which should expose refractive index difference in ER, FSR and interferometric peaks, accord-

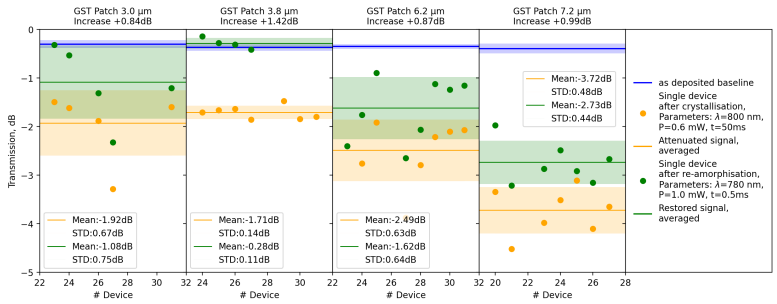


Figure 3.7: Restoration of the signal, measured at the peak of transmission window, after quenching re-amorphisation of GST

ing to 2.2.3.

The Figure of Merit in this kind of measurement is the **E**xinction **R**atio, which is directly connected to the attenuation of the signal in the GST loaded structure (described previously in 2.2.3). This measurement was not affected by the misalignment or weak signal, though its precision was governed by the noise level of Photodiode. On this step, the sufficient difference in GST state was observed while varying the parameters of switching (Fig.3.8). This allowed choosing optimal working point for laser-induced crystallisation.

Further endeavours were done towards fine tuning of re-amorphisation process as well. As it was mentioned earlier, amorphisation requires short exposure to high power radiation. In this situation the risks of burning the material instead of re-amorphising it is very high. The transmission measurements could not provide enough precision for distinguishing between these states of GST, while with interferometry the difference manifested in ER and peak shift (Fig.3.9). It allowed to choose operation regions and proceed to further optimization.

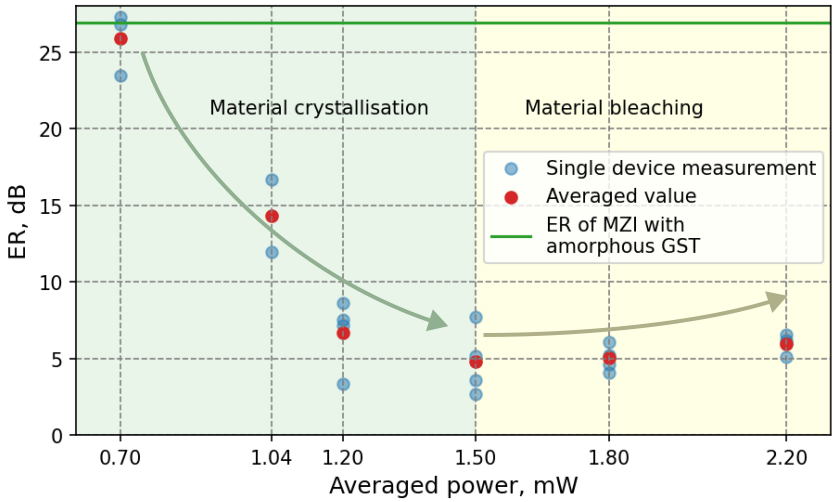


Figure 3.8: ER of GST-loaded MZI. Varying the switching parameters, different states of GST were acquired. Left part of the graph represents the increase of attenuation in GST loaded arm due to the growth of crystalline fraction. Right part represents start of *burning* of the material under high power.

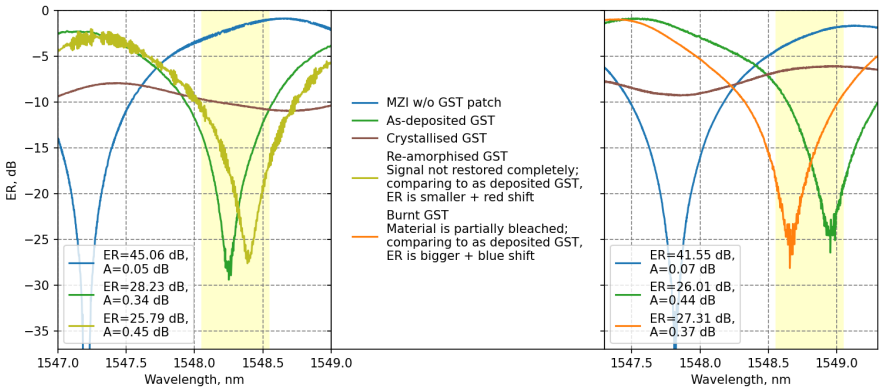


Figure 3.9: Experimental evaluation of the switching. Quenching amorphisation restores the transmission almost to "as deposited" level, whereas burning of the material manifests in partial bleaching and rise of ER **above** as-deposited level. Note, that the devices had different arm difference, therefore FSR and peak shifts must not be compared directly.

## 3.4 Results and discussion

### Measurement accuracy

Characteristics of GST-loaded waveguide structure were evaluated via direct transmission measurements and via incorporating into MZI structure. Both methods proved to be useful, nevertheless, interferometric measurements showed prominently bigger SNR and allowed measurements of small signal attenuation under 1 dB (Fig. 3.12), which was not available with backloops (Fig. 2.3b).

### Switching efficiency

The refinement of the setup levered the switching parameters' precision, which was pivotal for the fine-tuning. Given the refined switching evaluation via interferometry, we were able to choose optimal switching parameters (3.8), acquiring the effective signal attenuation of 7.5 dB in a GST loaded structure of length 4μm.

### Simulation comparison

The aforementioned results of switching are partly contradictory to the simulation, the result of which was presented earlier in Fig. 3.3b. This contradiction arises from the fact, that the materials expose different properties being handled in a structure. For the simulation we used the material data (refractive index), which was acquired via

| Name | Shift, nm | ER, dB | A, dB |
|---|---|---|---|
| w/o GST | 0 | 36.2 | 0.1 |
| amorph | 0.68 | 32.8 | 0.2 |
| cryst1 | 1.65 | 23.5 | 0.6 |
| cryst2 | 2.2 | 11.2 | 2.5 |
| cryst3 | 2.69 | 3.1 | 7.5 |

Table 3.1: Parameters of interferometric picture.

examination of thin filmed as-deposited and annealed GST. In experiment time-bounded laser impact is not consistent and prolonged enough to form the stable trigonal structure, therefore GST stays in one of numerous intermediate states (Wang *et al.* (2020)). Dictated by atomic arrangements, its optical and electrical properties are different, therefore full correspondence was not awaited. The **gradual change of the GST state** was clearly observed in interferometric pattern (Fig.3.10) with the red shift and curve flattening. The characterising parameters are put in Table 3.1.

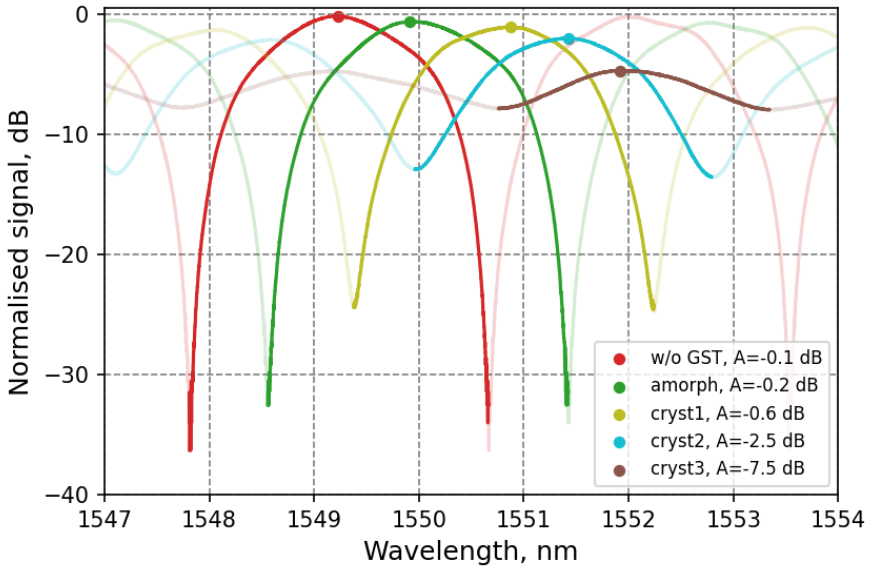


Figure 3.10: MZI spectra before and after GST switching, compared to the MZI without GST patch in general. Attenuation (A) in GST arm is derived from the Extinction Ratio (ER) of the MZI according to 2.2.3. *cryst1-2-3* stays for different levels of crystallisation.

In regard of interferometry simulation, bigger correspondence is noted. The comparison is presented in Fig. 3.11. This measurement represents the MZI with the arm difference of 400 μm. The GST patch of length 4 μm is firstly in the as deposited amorphous state, then it is crystallised with high power laser. As expected, the decrease of FSR and red shift of interferometric peaks is observed due to rise of effective index with crystallisation, and the attenuation in the patch manifests in the decrease of ER. The characteristic values are close to the result of the simulation, though the effects of the GST patch are much less pronounced.

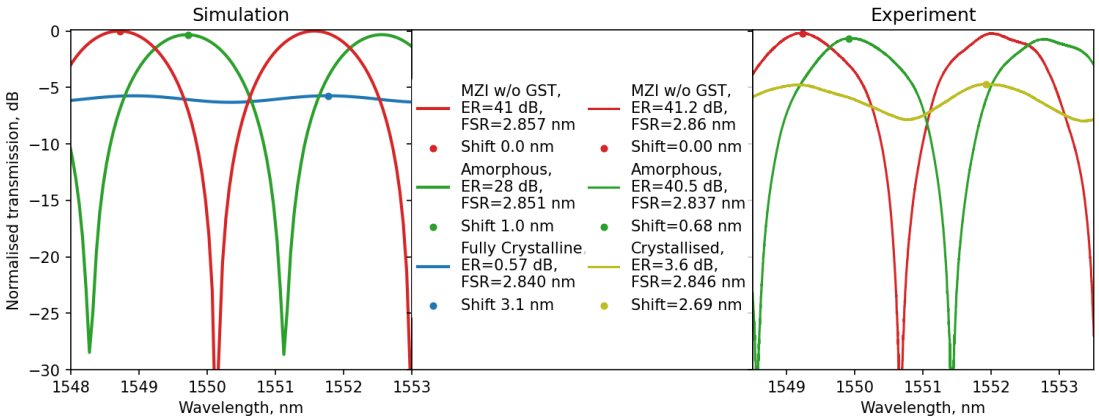


Figure 3.11: Simulation VS Experiment comparison are done based on red shift and ER. The contrast between amorphous and crystalline states are very pronounced and correspond to the expected values. However, difference from the MZI with no GST at all is not as big as expected.

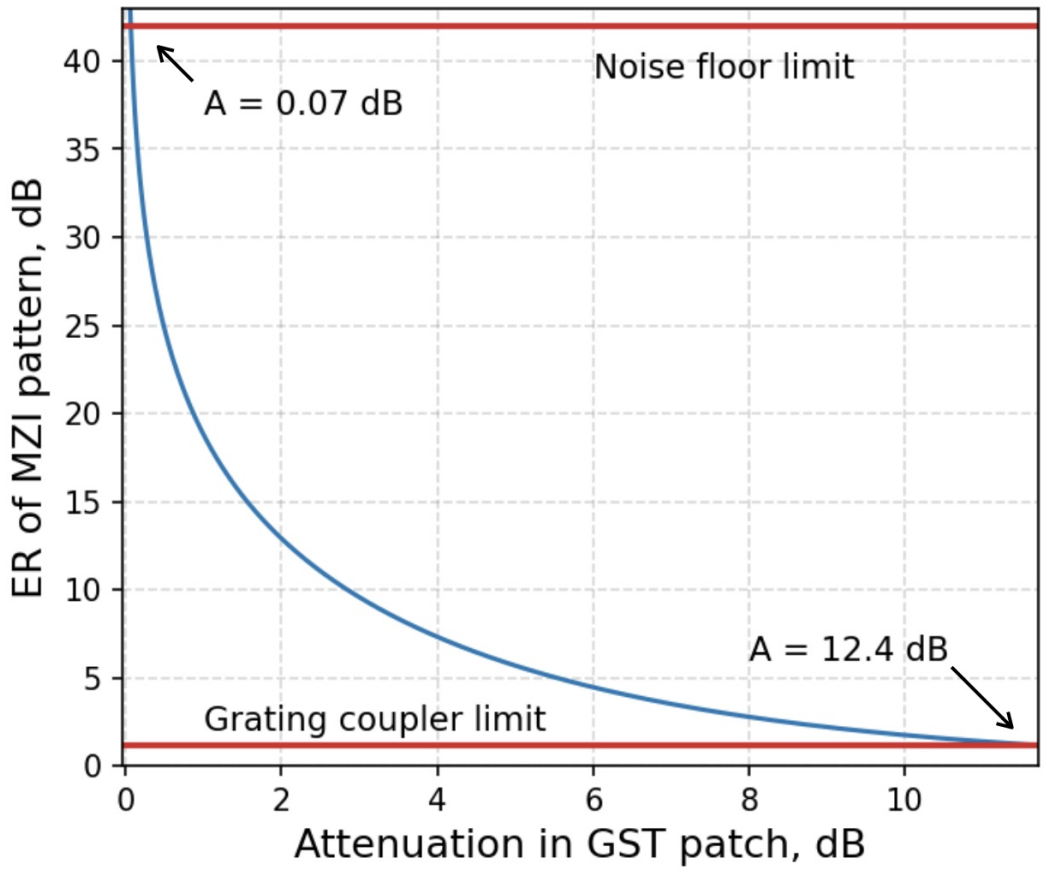


Figure 3.12: Attenuation in the GST-loaded structure in the MZI arm manifests in the ER. The nonlinear connection provides high sensitivity in range of low attenuation, with the lower boundary dictated by noise floor of the recording system.

# CHAPTER 4

# Conclusion

Phase change materials (PCMs) hold significant potential for photonic computing applications. When PCM is incorporated into photonic structures, its treatment induces moderate changes in the optical properties of the system. However, at the nanoscale, their behavior can differ from bulk material properties. Therefore, it is essential to evaluate the optical properties of the materials within the complete photonic structures to ensure accurate performance assessments.

In this work, the fundamental building block of the PCM-incorporating crossbar array – namely, the PCM-loaded waveguide – was examined. The effect of laser switching on the optical properties of this structure was evaluated through transmission and interferometric measurements. By offering a method of experimental validation of the structure performance, this research support the development of PCM switching techniques, which is pivotal for programming of PCM-based computing units. Proposed MZI scheme proved to be beneficial in several regards:

- It doesn't need to be referenced, which eliminates the systematic measurement error. ER provides comprehensive information about relative signal attenuation in the structure of interest.
- Nevertheless, usage of reference structures makes this method more versatile, allowing evaluating further parameters. Referencing to an MZI without GST patch on it provides info about peak shift and change of real part of effective refractive index, while referencing to Grating Couplers allows evaluation of insertion losses of the structure.
- This method is sensitive enough to measure slight signal attenuation due to non-linear dependency of ER (Fig. 3.12). It allows evaluation of attenuation in amorphous GST or recognising between amorphous and bleached material (Fig. 3.9), which was falling below the sensitivity limit for transmission measurements with backloops due to the overtaking systematic referencing error.

- It allowed evaluation of the structure under condition of low signal or misalignment, which simplified the automated measurements.
- The accuracy of this measurement is higher (SNR up to 100), which means it provides reliable result with less acquired data.

The limitations of this method are connected to the characteristics of the signal recording and are depicted in the Fig. 3.12. The noise floor of PD bounds the highest measurable limit of the ER: in the scope of this work, it stayed within $\mathrm{ER_{max}}$ = 42 dB, which corresponds to $\mathrm{A_{min}}$ = -0.07 dB signal attenuation in a structure. The lowest measurable ER was restricted with the ripples, arousing while coupling. Using the Grating Couplers it stayed at the level of $\mathrm{ER_{min}}$ = 1.2 dB, which made the maximal measurable attenuation $\mathrm{A_{max}}$ = -12.4 dB. Taking into account the considerations from 3.4, this range is suitable for validation of the attenuation in small GST patches after laser switching. The further extensions could be made with the lowering the noise floor and incorporating coupling systems with more flattened transmission window. Additionally, the further methodologies for investigation the crystallisation process in GST might come into focus for acquisition of advancement in switching techniques.

# REFERENCES


1. **Abdollahramezani, S.**, **O. Hemmatyar**, **H. Taghinejad**, **A. Krasnok**, **Y. Kiarashinejad**, **M. Zandehshahvar**, **A. Alù**, and **A. Adibi** (2020). Tunable nanophotonics enabled by chalcogenide phase-change materials. *Nanophotonics*, **9**(5), 1189–1241. URL https://doi.org/10.1515/nanoph-2020-0039.

2. *Optical Fiber and Data Centers: Powering the Digital Infrastructure* (retrieved: 2024-06-01). URL https://www.hfcl.com/blog/optical-fiber-and-data-centers.

3. **Ben-Nun, T.** and **T. Hoefler** (2019). Demystifying parallel and distributed deep learning: An in-depth concurrency analysis. *ACM Comput. Surv.*, **52**(4). ISSN 0360-0300. URL https://doi.org/10.1145/3320060.

4. **Brückerhoff-Plückelmann, F.**, **J. Feldmann**, **H. Gehring**, **W. Zhou**, **D. Wright**, **H. Bhaskaran**, and **W. Pernice** (2022). Broadband photonic tensor core with integrated ultra-low crosstalk wavelength multiplexers. *Nanophotonics*, **11**.

5. **de Lima, T. F.**, **B. J. Shastri**, **A. N. Tait**, **M. A. Nahmias**, and **P. R. Prucnal** (2017). Progress in neuromorphic photonics. *Nanophotonics*, **6**(3), 577–599. URL https://doi.org/10.1515/nanoph-2016-0139.

6. **Di Pasquale, F.**, **F. Meli**, **E. Griseri**, **A. Sguazzotti**, **C. Tosetti**, and **F. Forghieri**, 25-ghz spacing all-raman transmission of 192 wdm channels at 10.66 gb/s over 30/spl times/22 db of tw-rs fiber. *In OFC 2003 Optical Fiber Communications Conference, 2003.*, volume 1. 2003.

7. ECOC (2023). *22.9 Pb/s Data-Rate by Extreme Space-Wavelength Multiplexing*. 2023.

8. **Faneca Ruedas, J.**, **T. Domínguez Bucio**, **F. Gardes**, and **A. Baldycheva** (2020). O-band n-rich silicon nitride mzi based on gst. *Applied Physics Letters*, **116**, 093502.

9. **Feldmann, J.**, **N. Youngblood**, **M. Karpov**, **H. Gehring**, **X. Li**, **M. Stappers**, **M. Le Gallo**, **X. Fu**, **A. Lukashchuk**, **A. S. Raja**, **J. Liu**, **C. D. Wright**, **A. Sebastian**, **T. J. Kippenberg**, **W. H. P. Pernice**, and **H. Bhaskaran** (2021). Parallel convolutional processing using an integrated photonic tensor core. *Nature*, **589**(7840), 52–58. ISSN 1476-4687. URL http://dx.doi.org/10.1038/s41586-020-03070-1.

10. **Feng, W.-c.** and **S. Xiao**, To gpu synchronize or not gpu synchronize? *In 2010 IEEE International Symposium on Circuits and Systems (ISCAS)*. 2010.

11. **Harmgarth, N.**, **F. Zörner**, **P. Liebing**, **E. Burte**, **M. Silinskas**, **F. Engelhardt**, and **F. T. Edelmann** (2017). Molecular precursors for the phase-change material germanium-antimony-telluride, ge2sb2te5 (gst). *Zeitschrift für anorganische und allgemeine Chemie*, **643**.

12. **Jouppi, N. P.** (2017). In-datacenter performance analysis of a tensor processing unit. *SIGARCH Comput. Archit. News*, **45**(2), 1–12. ISSN 0163-5964. URL https://doi.org/10.1145/3140659.3080246.

13. **Karpov, I.**, **D. Kencke**, **D. Kau**, **S. Tang**, and **G. Spadini** (2010). Phase change memory with chalcogenide selector (pcms): Characteristic behaviors, physical models and key material properties. *MRS Proceedings*, **1250**.

14. **Kim, K.-H.** and **C.-S. Jeong** (2023). Optimizing single dgx-a100 system: Overcoming gpu limitations via efficient parallelism and scheduling for large language models. *Applied Sciences*, **13**, 9306.

15. **Lankhorst** (2005). Low-cost and nanoscale non-volatile memory concept for future silicon chips. *Nat. Mater.*.

16. **Miller, D. A. B.** (2017). Attojoule optoelectronics for low-energy information processing and communications. *Journal of Lightwave Technology*, **35**(3), 346–396.

17. **Mohseni, M.** and **A. H. Novin** (2023). A survey on techniques for improving phase change memory (pcm) lifetime. *Journal of Systems Architecture*, **144**, 103008. ISSN 1383-7621. URL https://www.sciencedirect.com/science/article/pii/S138376212300187X.

18. **Nevzorov, A.**, **V. Mikhalevsky**, **N. Eliseev**, **A. Kiselev**, **A. Burtsev**, **V. Ionin**, **A. Maliutin**, **D. Khmelenin**, **V. Glebov**, and **A. Lotin** (2023). Two-stage conductivity switching of gst thin films induced by femtosecond laser radiation. *Optics Laser Technology*, **157**, 108773. ISSN 0030-3992. URL https://www.sciencedirect.com/science/article/pii/S0030399222009197.

19. **Park, S. H.** and **K. Han** (2018). Methodologic guide for evaluating clinical performance and effect of artificial intelligence technology for medical diagnosis and prediction. *Radiology*, **286**(3), 800–809. PMID: 29309734.

20. **Parra, J.**, **I. Olivares**, **A. Brimont**, and **P. Sanchis** (2021). Toward nonvolatile switching in silicon photonic devices. *Laser & Photonics Reviews*, **15**(6), 2000501. URL https://onlinelibrary.wiley.com/doi/abs/10.1002/lpor.202000501.

21. **Pirovano, A.**, **A. Lacaita**, **A. Benvenuti**, **F. Pellizzer**, and **R. Bez** (2004). Electronic switching in phase-change memories. *Electron Devices, IEEE Transactions on*, **51**, 452 – 459.

22. **Ríos, C.**, **Y. Zhang**, **M. Y. Shalaginov**, **S. Deckoff-Jones**, **H. Wang**, **S. An**, **H. Zhang**, **M. Kang**, **K. A. Richardson**, **C. Roberts**, **J. B. Chou**, **V. Liberman**, **S. A. Vitale**, **J. Kong**, **T. Gu**, and **J. Hu** (2021). Multi-level electro-thermal switching of optical phase-change materials using graphene. *Advanced Photonics Research*, **2**(1), 2000034. URL https://onlinelibrary.wiley.com/doi/abs/10.1002/adpr.202000034.

23. **Ríos Ocampo, C.**, **M. Stegmaier**, **P. Hosseini**, **D. Wang**, **T. Scherer**, **D. Wright**, **H. Bhaskaran**, and **W. Pernice** (2015). Integrated all-photonic non-volatile multi-level memory. *Nature Photonics*, **9**, 725–732.

24. **Shen, Y.**, **N. C. Harris**, **S. Skirlo**, **M. Prabhu**, **T. Baehr-Jones**, **M. Hochberg**, **X. Sun**, **S. Zhao**, **H. Larochelle**, **D. Englund**, and **M. Soljačić** (2017). Deep learning with coherent nanophotonic circuits. *Nature Photonics*, **11**(7), 441–446. ISSN 1749-4893. URL https://doi.org/10.1038/nphoton.2017.93.

25. **Soldano, L.** and **E. Pennings** (1995). Optical multi-mode interference devices based on self-imaging: principles and applications. *Journal of Lightwave Technology*, **13**(4), 615–627.

26. **Wang, J.**, **L. Wang**, and **J. Liu** (2020). Overview of phase-change materials based photonic devices. *IEEE Access*, **8**, 121211–121245.

27. **Winzer**, **Neilson**, and **Chraplyvy**, *Fiber-optic transmission and networking: the previous 20 and the next 20 years*. Opt.Express, 2018.

28. **Wuttig, M.**, **H. Bhaskaran**, and **T. Taubner** (2017). Phase-change materials for non-volatile photonic applications. *Nature Photonics*, **11**, 465–476.

29. **Xu, R.**, **S. Taheriniya**, **A. P. Ovvyan**, **J. R. Bankwitz**, **L. McRae**, **E. Jung**, **F. Brückerhoff-Plückelmann**, **I. Bente**, **F. Lenzini**, **H. Bhaskaran**, and **W. H. P. Pernice** (2023). Hybrid photonic integrated circuits for neuromorphic computing. *Opt. Mater. Express*, **13**(12), 3553–3606.

30. **Zhang, C.**, **P. Li**, **G. Sun**, **Y. Guan**, **B. Xiao**, and **J. Cong**, Optimizing fpga-based accelerator design for deep convolutional neural networks. *In Proceedings of the 2015 ACM/SIGDA International Symposium on Field-Programmable Gate Arrays*, FPGA '15. Association for Computing Machinery, New York, NY, USA, 2015. ISBN 9781450333153. URL https://doi.org/10.1145/2684746.2689060.